npj | Materials Degradation

www.nature.com/npjmatdeg

ARTICLE OPEN

Check for updates

Corrosion mechanism of an equimolar AlCoCrFeNi high-entropy alloy additively manufactured by electron beam melting

Kenta Yamanaka[1]✉, Hiroshi Shiratori[2,3], Manami Mori[4], Kazuyo Omura[1], Tadashi Fujieda[3], Kosuke Kuwabara[3] and Akihiko Chiba[1]

High-entropy alloys (HEAs) have emerged as a class of structural alloys with various attractive properties, and their application in additive manufacturing, which enables unprecedented thermal history and geometrical complexity, is promising for realising advanced materials. This study investigates the corrosion behaviour and passive film characteristics of an equimolar AlCoCrFeNi HEA additively manufactured by electron beam melting (EBM). Potentiodynamic polarisation in a 3.5 wt% NaCl solution revealed that the bottom part of the EBM specimen shows better corrosion performance than a conventionally prepared cast specimen in terms of both corrosion and passivation current density, while a continuous increase in the current density without any apparent passivity was observed during the anodic polarisation of the top part. The electrochemical impedance spectroscopic study indicated significant differences in the passive film characteristics between the specimens, and revealed an enhanced charge-transfer resistance and the formation of a more protective passive film of the bottom part. The elemental redistribution, in particular, the enrichment of Cr in the B2 phase during the post-melt high-temperature exposure of the alloy during EBM, was responsible for the improved stability of the passive film, retarding the selective dissolution of the B2 phase in the bottom part. These findings indicate that the microstructural evolution caused by 'in situ annealing' during the EBM process significantly influences the corrosion behaviour of the HEA.

npj Materials Degradation (2020)4:24; https://doi.org/10.1038/s41529-020-00127-4

INTRODUCTION

High-entropy alloys (HEAs) are multicomponent alloys composed of five or more elements in equimolar or near-equimolar proportions[1–3]. HEAs have many promising properties, such as significant solid-solution strengthening originating from severe lattice distortion[3,4], excellent strength–ductility balance[5], superior damage tolerance at cryogenic temperatures[6,7] and high wear resistance[8,9], thus drawing considerable attention from the materials science community. It has been claimed that due to the unique alloying concept, the high mixing entropy of these alloys stabilises the solid-solution phases, such as in face-centred cubic (FCC) and body-centred cubic (BCC) structures. However, it does not necessarily assure the formation of a simple solid solution and, indeed, some HEAs show complex microstructures with the formation of secondary or intermetallic phases within the matrix[10,11]. Thus, such alloys do not have high configurational entropies and are often generally termed as 'compositionally complex alloys' (CCAs)[12–14].

The corrosion characteristics of HEAs have been studied extensively[15–32]. Kumar et al.[20] revealed that a single-phase FCC $Al_{0.1}$CoCrFeNi HEA has a superior corrosion resistance to that of 304 stainless steel in a 3.5 wt% NaCl solution. Conversely, the corrosion resistance of HEAs with microstructural heterogeneities (i.e. CCAs) is often severely degraded when exposed to aqueous environments. Kao et al.[26] examined the electrochemical passivity of Al_xCoCrFeNi ($x = 0$, 0.25, 0.50 and 1.00) alloys in sulfuric acid. It was demonstrated that as the x value increased to 1.00, the microstructure varied from single-phase FCC to BCC/B2 (ordered BCC) duplex microstructures, leading to an inductance effect in the equivalent circuit for the severe dissolution of the Al- and Ni-rich phases.

Recently, additive manufacturing (AM) has garnered significant attention as it enables the production of components with complex geometries directly from 3D computer-aided design data. Some such geometries cannot otherwise be fabricated through conventional manufacturing routes, such as casting, powder metallurgy and/or plastic deformation. Electron beam melting (EBM) is a powder-bed-fusion (PBF) AM technology that has been applied to many metallic materials[33]. A high-energy electron beam used as an energy source for selectively melting a metal powder bed can effectively prevent the formation of critical defects, such as cracks and lack of fusion under optimal processing parameters, thus enabling the production of fully dense metal components with superior mechanical properties.

In a previous study, equimolar AlCoCrFeNi HEA components were successfully fabricated using EBM. The as-built specimens were verified to have better mechanical properties and specifically better plastic deformability than those of specimens of the same alloy prepared using a conventional casting technique[34–36]. This result indicates that the microstructural evolution during AM, which is considerably different from that in conventional manufacturing, could significantly affect the properties of AM components. However, the corrosion behaviours of additively manufactured HEAs have been rarely reported[36–40]. Studies on corrosion were conducted on the EBM-built AlCoCrFeNi HEA[36]; these revealed that the breakdown of passivity during

[1]Institute for Materials Research, Tohoku University, 2-1-1 Katahira, Aoba-Ku, Sendai 980-8577, Japan. [2]Department of Materials Processing, Graduate School of Engineering, Tohoku University, 6-6-11 Aramaki, Aoba-Ku, Sendai 980-8579, Japan. [3]Center for Technology Innovation—Materials, Research & Development Group, Hitachi, Ltd., 7-1-1 Ohmika-Cho, Hitachi 319-1292, Japan. [4]Department of General Engineering, National Institute of Technology, Sendai College, 48 Nodayama, Medeshima-Shiote, Natori 981-1239, Japan. ✉email: k_yamanaka@imr.tohoku.ac.jp

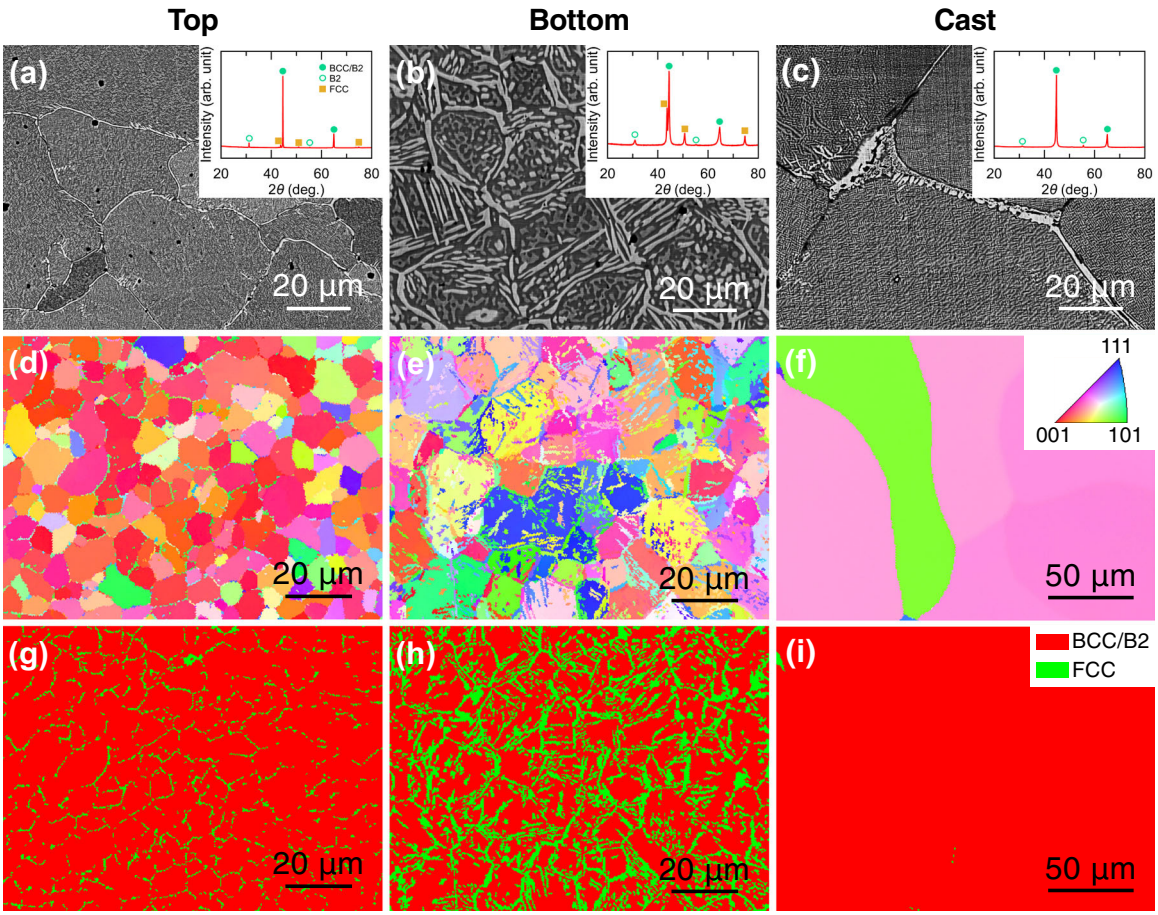

Fig. 1 Microstructures of the EBM and cast AlCoCrFeNi HEA specimens. a–c SEM-BSE images, **d–f** IPF maps and **g–i** phase maps obtained from the cross-section perpendicular to the build direction at the **a**, **d**, **g** top and **b**, **e**, **h** bottom sections of the EBM specimen and **c**, **f**, **i** cast specimen. The corresponding XRD patterns are also indicated in **a–c**.

potentiodynamic polarisation measurements in artificial seawater occurred at a lower potential than that of the cast counterpart. However, the mechanism underlying the corrosion behaviour of the EBM materials has not been clarified yet.

A preheating procedure is unique to the EBM process; it is important to suppress the charge accumulation of powder particles and the resulting 'powder explosion' (namely, a 'smoke' event). Furthermore, residual stresses, which can cause the distortion and failure of components in other AM processes such as selective laser melting (SLM)[33,41], are significantly reduced in the final products processed by EBM. However, this procedure makes EBM a completely hot process. The long build time at elevated temperatures allows microstructural evolutions such as grain growth[42] and phase transformation[43,44] during their fabrication. This 'in situ annealing' feature notably differentiates EBM from other PBF processes, such as SLM, in which the selective melting of raw powder is generally conducted without preheating.

In this study, the corrosion behaviours of an equimolar AlCoCrFeNi HEA prepared by EBM were examined at different build heights to examine the effect of post-melt high-temperature exposure. The mechanisms underlying the corrosion performance of the EBM specimen are discussed based on detailed microstructural examinations.

RESULTS

Microstructures

Figure 1 depicts the typical microstructures of the studied AlCoCrFeNi HEA specimens, as observed by scanning electron microscopy (SEM), X-ray diffraction (XRD) and electron backscatter diffraction (EBSD) measurements. The back-scattered electron (BSE) images reveal the characteristic modulated structure of the matrices of all the samples, as shown in Fig. 1a–c. The XRD data indicate that the specimens are primarily composed of both ordered (B2) and disordered BCC phases. Thus, the modulated structures correspond to the duplex microstructure of the BCC and B2 phases (hereafter, this is denoted as the 'BCC/B2 matrix'). The modulated structure in the EBM specimens was markedly coarsened at the bottom section, while it was finer at the top section (with less than 200-nm width), as compared with that of the cast specimen. EBSD measurements revealed that in the EBM specimens, the ⟨100⟩ direction of the BCC/B2 matrix was strongly orientated along the build direction in the top part (Fig. 1d), which can be ascribed to the directional solidification along the building direction. Conversely, a more random orientational distribution, but a weaker $\langle 100 \rangle_{BCC/B2}$ texture, than that of the top part, was observed in the bottom part of the EBM specimen (Fig. 1e). Remarkably, the EBM specimens showed the evolution of the FCC phase at the grain boundaries of the BCC/B2 grains with an increase in the post-solidification period; the FCC-phase fraction (~30%) was considerably higher in the bottom part (Fig. 1h) than in the top part (Fig. 1g), where this fraction was almost negligible. The bright contrast for the FCC phase in the BSE images indicates that the average atomic number for the FCC phase is higher than that for the BCC/B2 matrix (in other words, it contains less Al). In contrast, the cast specimen almost exclusively showed a BCC/B2 matrix; it did not exhibit any specific strong texture (Fig. 1f), and the FCC phase was hardly identified (Fig. 1i). Finally, the inverse

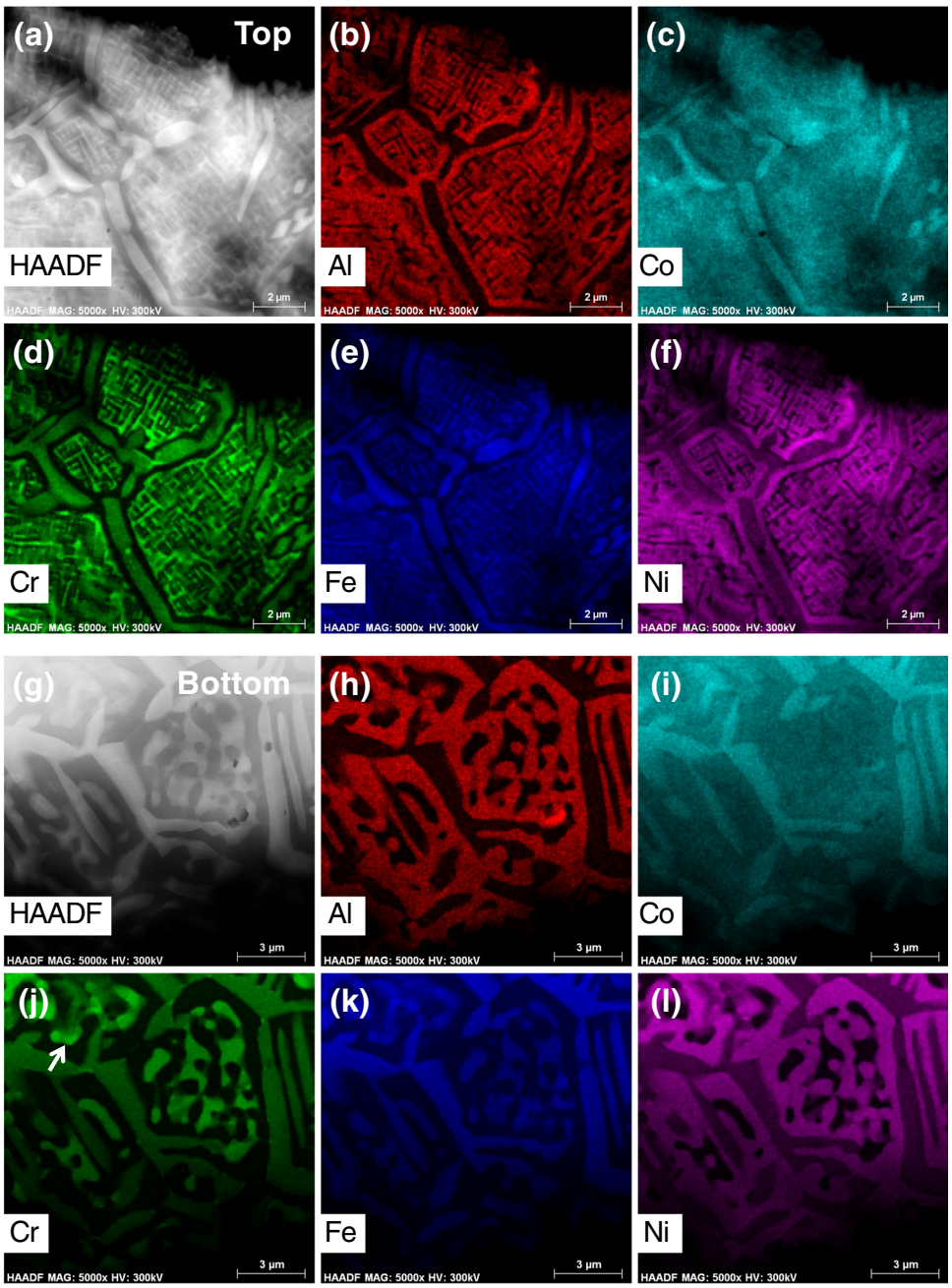

Fig. 2 Nanoscale elemental distributions of the EBM specimen. a, g HAADF-STEM image and the corresponding EDS elemental maps of **b, h** Al, **c, i** Co, **d, j** Cr, **e, k** Fe and **f, l** Ni for the **a–f** top and **g–l** bottom sections of the EBM specimen.

pole figure maps show no significant grain-size difference between the two parts of the EBM specimens, while the cast specimens are found to have coarser grains. The average grain sizes of the BCC/B2 matrix of the EBM and cast specimens are ~10 and 300 μm, respectively.

Figure 2 depicts the results of scanning transmission electron microscopy (STEM) observations at different build heights of the EBM specimen. The high-angle annular dark-field (HAADF)-STEM images in Fig. 2a, g captured nanoscale elemental partitioning at each build height. The corresponding energy-dispersive X-ray spectroscopy (EDS) elemental mapping indicated that Al and Ni were preferentially distributed to the B2 phase, whereas the BCC phase contained a higher fraction of Cr and Fe, as shown in Fig. 2b, f and d, e, respectively. Although the elemental partitioning of Co between the BCC and B2 phases was not obvious in Fig. 2c, it was partitioned preferentially into the FCC phase, together with Cr and Fe, which was dominantly observed at the grain boundaries of the BCC/B2 matrix. A similar phase separation was observed in the bottom part, although the microstructure was coarsened, as shown in Fig. 2h–l. However, the results of the quantitative STEM-EDS analysis (Table 1) clarified the difference in chemical composition in the BCC/B2 matrix. Namely, the BCC phase at the top part has higher Cr and lower Ni contents than in the bottom counterpart, but the BCC phase at the bottom part still has a Cr content of 27.65 at.%. Although the chemical composition of the B2 phase is similar between the top and bottom samples, the B2 phase at the top part contained a much lower Cr content of ~4 at% compared with the bottom part, which was as high as ~7 at%. Accordingly, the elemental partitioning within the BCC/B2 matrix resulted in the difference

Table 1. Chemical compositions (average ± 3σ) of the constitutive phases in the EBM specimen (at%), as determined by STEM-EDS analysis.

Specimen	Phase	Al	Co	Cr	Fe	Ni
Top	BCC	0.21 ± 0.15	19.72 ± 2.37	46.09 ± 4.36	30.42 ± 3.23	3.56 ± 0.72
	B2	17.45 ± 1.13	24.66 ± 2.98	4.00 ± 0.70	16.83 ± 2.06	37.06 ± 4.24
	FCC	2.23 ± 1.10	28.25 ± 7.37	21.85 ± 5.55	31.93 ± 7.42	15.75 ± 5.40
Bottom	BCC	0.57 ± 0.16	18.00 ± 2.02	49.01 ± 4.45	28.84 ± 2.91	3.58 ± 0.59
	B2	17.44 ± 1.03	24.01 ± 2.75	7.02 ± 0.89	15.16 ± 1.75	36.37 ± 4.00
	FCC	1.45 ± 0.17	26.37 ± 2.67	27.65 ± 2.47	31.49 ± 2.99	13.04 ± 1.39

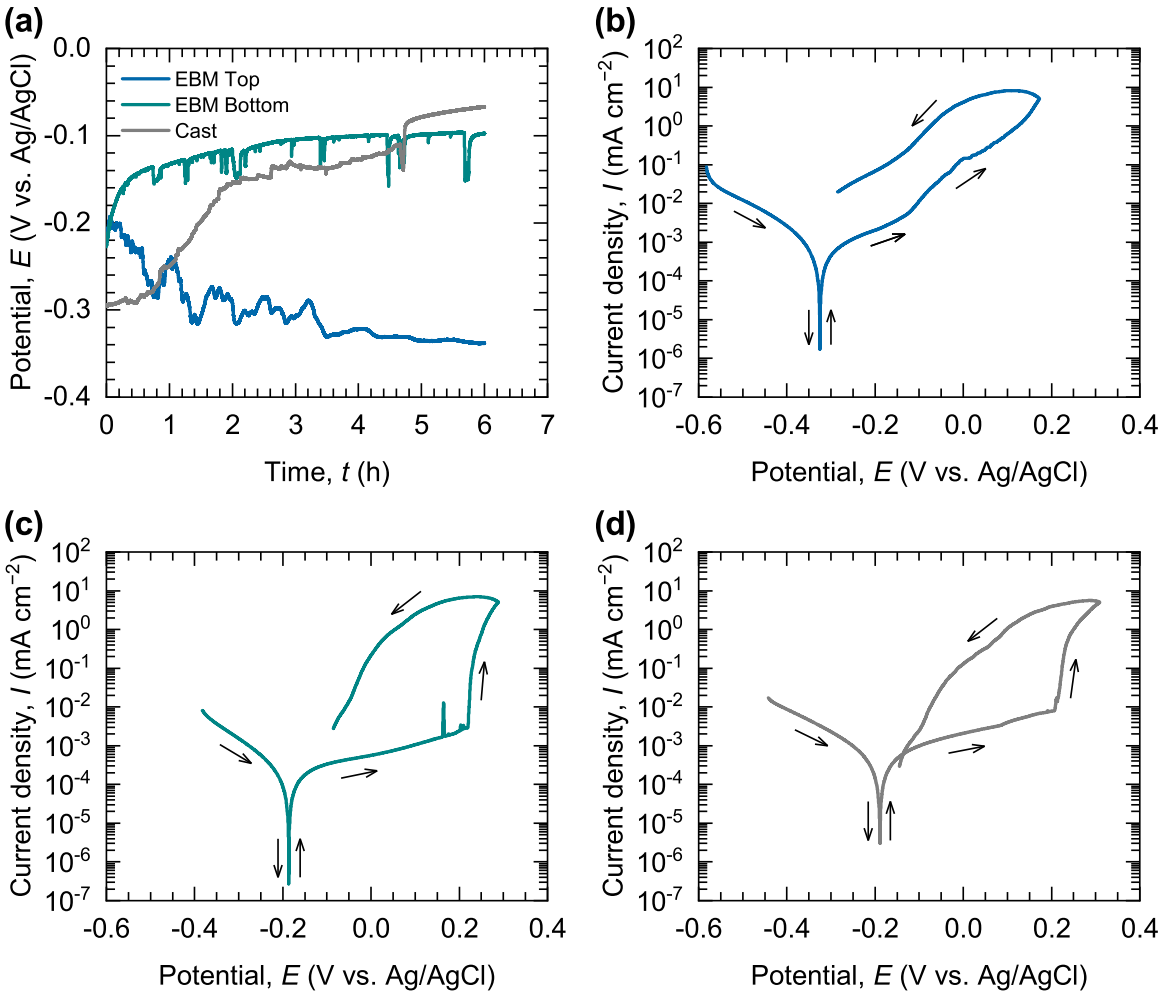

Fig. 3 Corrosion behaviour of the EBM and cast AlCoCrFeNi HEA specimens in a 3.5 wt% NaCl solution. a Evolution of E_{oc} as a function of immersion time and typical cyclic potentiodynamic polarisation curves for the **b** top and **c** bottom sections of the EBM specimen and **d** cast specimen.

in the lattice parameters between the BCC and B2 phases, causing the asymmetric BCC/B2 peaks in the XRD pattern (Fig. 1b). The FCC phase at both build heights showed an almost identical chemical composition. Furthermore, Cr-enriched particles were identified at the BCC/B2 interfaces of the bottom specimen (see the arrow in Fig. 2j for instance). This phase was enriched with Cr and contained Co and Fe, indicating that the small amount of nanosized particles in the bottom specimen consisted of the σ phase of an intermetallic compound, (Co, Fe)Cr[45]. The cast specimen exhibited an elemental partitioning tendency that is identical to the EBM specimen and is consistent with the literature[46,47]; however, the modulated BCC/B2 structure was finer than those in the EBM specimen, and the fraction of the FCC phase was negligibly low (Supplementary Fig. 1).

Potentiodynamic characteristics

Figure 3a depicts the variations in the open-circuit potential (E_{oc}) of the EBM and cast specimens immersed in a 3.5 wt% NaCl solution at room temperature. E_{oc} is the measured voltage difference between the working electrode and the reference electrode when no current flows through the electrolytic cell, and it reflects the surface states of the metal when immersed in an electrolyte. Generally, with increasing immersion time, the E_{oc} of

the bottom and cast specimens showed a gradual shift to positive values to attain stable surfaces with the electrolyte, indicating passivation during immersion. Conversely, the potential for the top part of the EBM specimen decreased continuously with increasing immersion time. The fluctuations in E_{oc} indicate that the sample surface was not stable in the corrosive environment. The final stabilised potential after 6-h immersion of the top specimen was much lower than those for the other specimens studied.

Figure 3b–d depicts the typical cyclic polarisation curves obtained for the EBM and cast AlCoCrFeNi HEA specimens in a 3.5 wt% NaCl solution at room temperature. The arrows indicate the potential scan direction during cyclic polarisation measurements. While the current density of the top part increased continuously and did not show a clear passivity in the anodic region (Fig. 3b), the bottom counterpart demonstrated an obvious passivation (Fig. 3c). The cast specimen also showed the passivation in anodic polarisation, as shown in Fig. 3d. Notably, the passive current density for the bottom sample was apparently lower than that of the cast specimen. A positive hysteresis, which shows that the current density of the reverse scan exceeds that of the forward scan, was identified for all the specimens examined in this study, indicating that all the specimens were susceptible to pitting corrosion. The cast specimen demonstrated a repassivation tendency during cyclic polarisation, where the current density during the reverse scan decreased to reach a repassivation potential at which the current density corresponds to the passive current density value. Unlike the previous research on the corrosion behaviour of as-cast AlCoCrFeNi-based HEAs[48], the repassivation potential was not always realised in the present cast specimen. Conversely, the EBM samples did not reach repassivation at both build heights. The area of the positive hysteresis loop is related to the pitting corrosion rate during the cycle[49]; a larger area under the positive hysteresis loop for the bottom part of the EBM specimen indicates a more rapid growth of the nucleated pits upon their surfaces than that of the cast specimen. The metastable pits were observed at the bottom part of the EBM specimen.

The corrosion potential (E_{corr}) and corrosion current density (i_{corr}) values, which were obtained from the polarisation curves by Tafel fitting, are presented in Table 2. The results indicate that the cast specimen shows the highest E_{corr}, while the top part of the EBM specimen shows a much lower E_{corr} of −326 mV vs. Ag/AgCl. The bottom section shows an intermediate E_{corr}. Conversely, the lowest i_{corr} value was observed for the bottom specimen, followed by the cast counterpart. The top part showed the highest i_{corr} value among the specimens. Furthermore, the pitting potential (E_{pit}), where the current density suddenly increased after showing the passive region, was almost the same (approximately 210 mV vs. Ag/AgCl) between the cast and EBM sample in the bottom section (Table 2).

In summary, the bottom part of the EBM specimen has the best corrosion resistance both in terms of corrosion rate and passivity, while a more rapid growth of pits than that of the cast specimen was expected during cyclic polarisation.

Table 2. Electrochemical parameters obtained by potentiodynamic polarisation tests for the EBM and cast AlCoCrFeNi HEA specimens in a 3.5 wt% NaCl solution at room temperature.

Specimen	E_{corr} (mV vs. Ag/AgCl)	i_{corr} (mA cm^{-2})	E_{pit} (mV vs. Ag/AgCl)
EBM Top	−326 ± 16	0.67 ± 0.09	–
EBM Bottom	−202 ± 17	0.22 ± 0.05	209 ± 10
Cast	−160 ± 38	0.36 ± 0.19	214 ± 6

Corroded surfaces

The surface morphologies of the top and bottom sections of the EBM specimens after the potentiodynamic polarisation tests are depicted in Fig. 4a, b, respectively. It is evident that the corrosion attack (namely, pitting corrosion) was localised in both samples, which is consistent with the results of cyclic polarisation tests, although the number of pits was much lower in the bottom part than in the others. The magnified images in Fig. 4d, e reveal that the BCC/B2 matrix of the EBM-built samples was susceptible to selective dissolution, while the grain-boundary FCC phase remained intact, without showing significant corrosion attack.

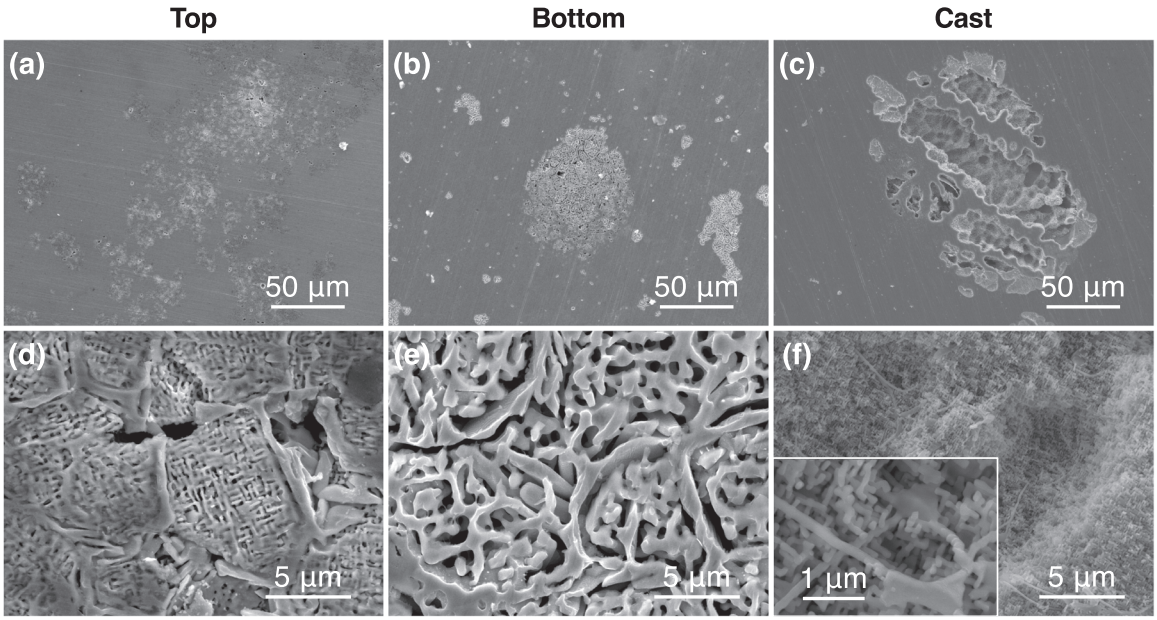

Fig. 4 SEM images of the sample surfaces after the polarisation tests in a 3.5 wt% NaCl solution at room temperature. a, **d** Top and **b**, **e** bottom sections of the EBM sample and **c** its cast counterpart. The magnified images of **a**–**c** are shown in **d**–**f**, respectively.

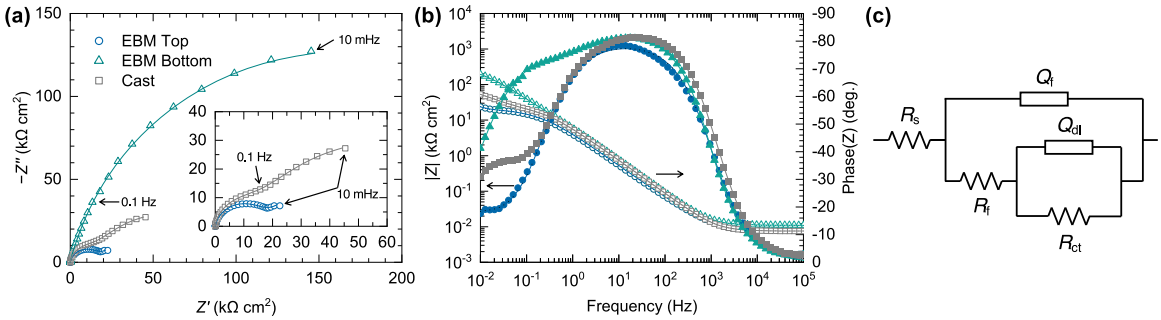

Fig. 5 EIS results of the EBM and cast AlCoCrFeNi HEA specimens at E_{oc} in a 3.5 wt% NaCl solution at room temperature. a Nyquist plots, **b** Bode plots and **c** the EEC employed for fitting the EIS data.

Table 3. Electrochemical parameters obtained from EIS measurements for the EBM and cast AlCoCrFeNi HEA specimens in a 3.5 wt% NaCl solution for 6 h at room temperature.

Specimen	R_s (Ω cm^2)	Q_f (μF s^{n-1} cm^{-2})	n_f	R_f (kΩ cm^2)	Q_{dl} (μF s^{n-1} cm^{-2})	n_{dl}	R_{ct} (kΩ cm^2)	R_p (kΩ cm^2)	C_{eff} (μF cm^{-2})
EBM Top	8.628	47.57	0.8863	17.80	700.7	0.7037	22.59	40.39	102.94
EBM Bottom	11.03	27.85	0.9277	24.00	12.33	0.7246	303.68	327.68	43.52
Cast	7.552	29.52	0.9264	20.05	130.5	0.7154	81.74	101.79	45.36

Consequently, network-like porous surfaces were created. A similar localised corrosion characteristic was observed in the cast sample, although the pit size was much larger than those of the EBM counterparts (Fig. 4c). Figure 4f suggested that the selective dissolution also occurred in the cast specimen.

Surface film structures

Figure 5a, b, respectively, depicts the representative Nyquist and Bode diagrams for the EBM and cast specimens after 6 h of immersion in a 3.5 wt% NaCl solution at room temperature, as obtained by electrochemical impedance spectroscopy (EIS) at E_{oc}. All the Nyquist plots show semicircular arcs with their centres depressed below the *x*-axis, which can be usually attributed to charge transfer on an inhomogeneous surface[50]. It is evident that the bottom section of the EBM sample exhibits the largest diameter of the depressed semicircle, while double semicircles with reduced diameters are observed for the remaining two samples. In the Bode plots, in contrast, the absolute values of impedance are almost independent of the frequency at frequencies >10^3 Hz in all cases, where the phase angle approached −10°, indicating that the solution resistance did not vary considerably. However, significant differences between the specimens were identified at medium-to-low frequencies with phase angles approaching −90°.

The electrochemical characteristics of the passive film for each specimen were quantitatively evaluated by modelling and fitting the experimental impedance spectra with the equivalent electrical circuit (EEC). Because the large phase-angle peak in the Bode diagram (Fig. 5b) indicates the electrochemical system associated with at least two time constants, the EEC consists of two RC groups. An EEC used in this study is displayed in Fig. 5c. The model has been used for Al-containing, B2-structured CCA[19] and alloys sensitive to pitting corrosion[51,52]. In this model, R_s refers to the solution resistance. R_f and Q_f correspond to the resistance and capacitance of the passive film, respectively, whereas R_{ct} and Q_{dl} are the charge-transfer resistance and double-layer capacitance, respectively. A constant-phase element (CPE) was used to represent a shift from the ideal capacitor. As depicted in Fig. 5a, b, the simulated responses (solid lines) of the EEC in Fig. 5c agree well with the experimental results, indicating that the model is suitable for describing the passive film characteristics of the studied specimens in the 3.5 wt% NaCl solution.

Table 3 lists the obtained electrochemical parameters for each specimen. There is no significant difference in the R_s value. Notably, the top part of the EBM specimen showed the highest Q_f value among the studied specimens, while no significant variations in the n_f and R_f were noticed. On the other hand, the lowest Q_{dl} value was obtained for the bottom part, while a much higher value was obtained for the top part of the EBM specimen. The cast sample falls in the middle. Conversely, the R_{ct} showed the opposite tendency, with the bottom and bottom parts showing the highest and lowest R_{ct} values, respectively.

Surface chemistry

The survey X-ray photoelectron spectra (XPS) of the prepared specimens before and after immersion in a 3.5 wt% NaCl solution at room temperature show major peaks of the metals—the Al *2p*, Co *2p*, Cr *2p*, Fe *2p* and Ni *2p* peaks—as well as the O *1s* peak (Supplementary Fig. 2). High-resolution narrow-scan XPS profiles of the specimens are presented in Fig. 6. The chemical compositions of the outermost surfaces before and after the immersion tests, calculated from the XPS data, are shown in Supplementary Tables 1–3. Further, to clarify the distributions of metallic elements at the immersed surfaces, the relative distributions of the metallic components in the surface oxides before and after the immersion tests are detailed in Fig. 7 and presented in Supplementary Table 4. All the metallic elements of the studied multicomponent alloy existed in both metal and oxide forms at detectable depths, although the fraction of each state was different among the specimens. Overall, no significant differences were identified among the XPS profiles of the specimens before immersion. Among the constitutive elements, Al (Fig. 6a), Co (Fig. 6b), Cr (Fig. 6c) and Fe (Fig. 6d) preferentially existed in their oxidised states, although the metallic state was preferred for Ni (Fig. 6e). The O *1s* peaks could be deconvoluted into three peaks: O^{2-}, hydroxide (OH^-) and hydrates and/or adsorbed water (H_2O). Before immersion in the 3.5 wt% NaCl solution, the hydroxide component was dominant in all the specimens (Fig. 6f).

Conversely, the oxidised state (Al^{3+}) was preferential for Al after immersion (Fig. 6g). Although the top part of the EBM specimen that was immersed for 1 h showed the lowest amount of Al^{3+}

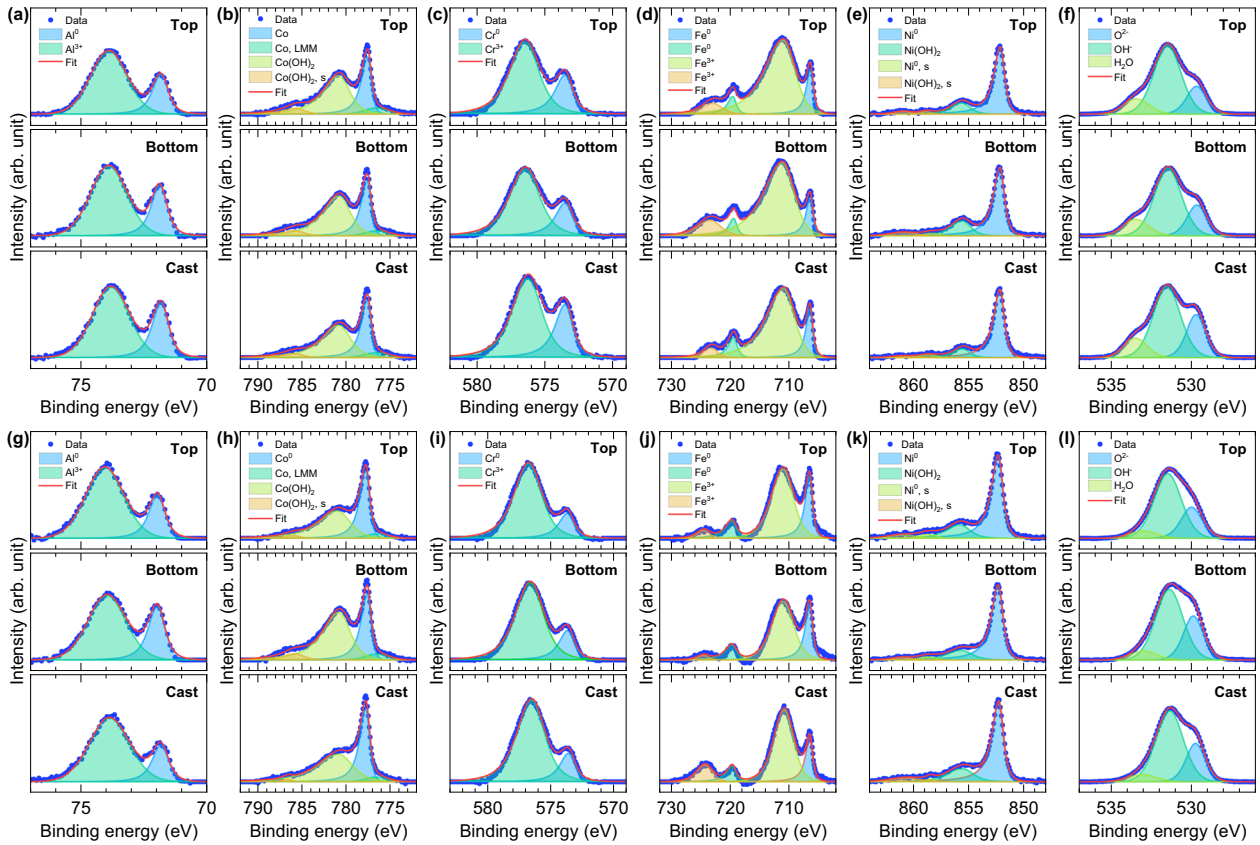

Fig. 6 XPS characterisation of the EBM and cast AlCoCrFeNi HEA specimens prepared in this study. High-resolution spectra for **a**, **g** Al *2p*, **b**, **h** Co *2p*, **c**, **i** Cr *2p*, **d**, **j** Fe *2p*, **e**, **k** Ni *2p* and **f**, **l** O *1s* collected **a**–**f** before and **g**–**l** after static immersion in a 3.5 wt% NaCl solution for 6 h at room temperature. The spectral deconvolution into component peaks is also shown.

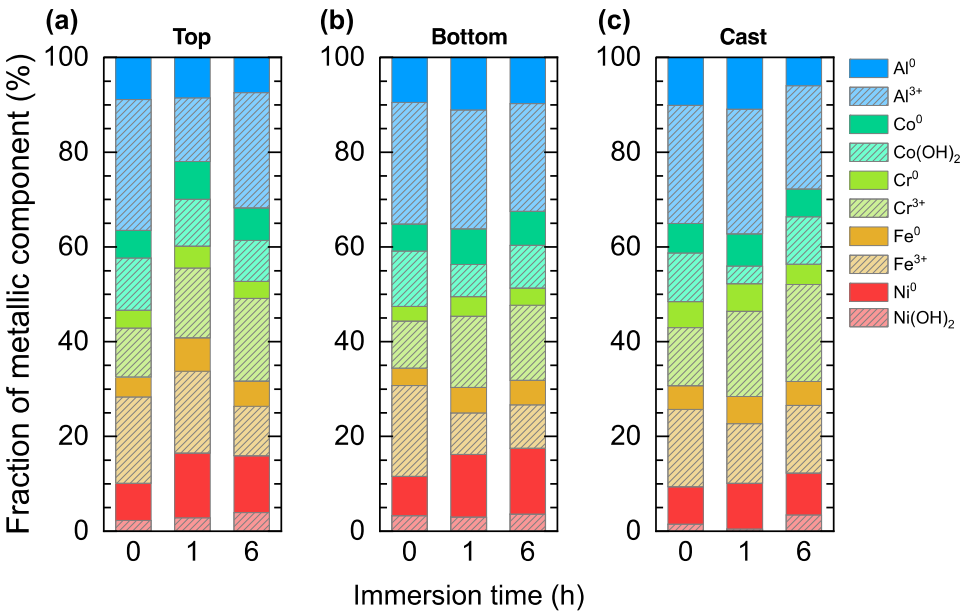

Fig. 7 Relative contents of metal species in the surface oxides of EBM and cast AlCoCrFeNi HEA specimens before and after immersion in a 3.5 wt% NaCl solution at room temperature. a Top and **b** bottom sections of the EBM sample and **c** its cast counterpart.

among the specimens, the significant variation between the samples disappeared after 6-h immersion (Fig. 7a). Remarkably, the increase of the Cr^{3+} component in the outermost surface oxide occurred in all the samples during immersion (Fig. 6h), which suggests the occurrence of the passivation process. Notably, the fraction of the Cr^{3+} component was almost identical for all the samples. The $Co(OH)_2$ compound remained as the preferred chemical state of Co after immersion (Fig. 6i), although a

progressive dissolution of $Co(OH)_2$ was observed in the bottom and cast samples at the early stage of immersion (at 1 h in Fig. 7b, c, respectively). Previously, the dissolution of cobalt has been observed in the passivation process of Co–Cr-based alloys[53–56]. Further, Fig. 6j, k revealed that Fe and Ni preferred Fe^{3+} and $Ni(OH)_2$, respectively, when immersed in the NaCl solution. Finally, immersion into the NaCl solution decreased the amount of the O^{2-} component, while the fraction of the OH^- ions increased (Fig. 6l). Overall, the results of the XPS analysis suggested no apparent difference in the surface chemistry/state between the samples after immersion in terms of the metal components or the state of oxygen, despite the variation in the corrosion behaviour between the samples.

DISCUSSION

Both the EBM and cast specimens consisted primarily of the duplex BCC/B2 matrix, which was formed directly from the melt[46]. In the EBM specimen, the modulated BCC/B2 matrix was developed preferentially at the top section, so that the $\langle 100\rangle_{BCC/B2}$ direction of the crystal was parallel to the build direction, whereas the bottom portion showed relatively random crystallographic orientations (Fig. 1). This indicates that as the EBM process proceeded, the microstructure tended to gradually transform into the stable $\langle 100\rangle_{BCC/B2}$ fibre texture during solidification. Conversely, coarsening of the modulated BCC/B2 structure occurred at the bottom part at the same time (Fig. 2), and the grain size of BCC/B2 increased slightly. Remarkably, the FCC phase was observed preferentially at the grain boundaries of the BCC/B2 grains. Although the formation of the grain-boundary FCC phase has been observed in AlCoCrFeNi-based HEAs produced by laser PBF techniques[57,58], the fraction of the FCC phase was much smaller than that at the bottom section of the EBM specimen. The results of the STEM-EDS mapping also imply the precipitation of a small amount of the Cr-enriched σ phase at the bottom section (Fig. 2). The coarsening of the modulated BCC/B2 structure, as well as the formation of the FCC and σ phases, can be explained by a solid-state phase transformation from the non-equilibrium microstructure formed just after solidification towards a thermally stable phase distribution[59] during the fabrication, because the EBM specimen was subjected to temperatures as high as the preheating temperature (950 °C) for a certain period (~13 h in this case). Obviously, the bottom part was more affected by the high-temperature exposure than the top part. The cast specimen, on the other hand, showed a microstructure comparable to that of the top part, because the cast specimen was not maintained at high temperatures. The microstructural evolution of the equiatomic AlCoCrFeNi HEA during EBM and casting is schematised in Fig. 8.

The most interesting finding of this study is the obvious difference in the corrosion behaviour along the build direction in the studied equiatomic AlCoCrFeNi HEA. The opposite tendency between the top and bottom parts was noticed in the E_{oc} measurements, as shown in Fig. 3a. The potentiodynamic polarisation measurements (Fig. 3b–d) revealed that the bottom part of the EBM specimen showed higher E_{corr} and lower i_{corr} values than the top part (Table 2). Notably, the passivation behaviour was also considerably different between the specimens, although all the studied samples were susceptible to pitting corrosion. Whereas the bottom part of the EBM specimen, as well as the cast specimen, showed passivity during anodic polarisation, no apparent passivation behaviour was identified in the polarisation curve in the top part of the EBM specimen. Notably, the lower passive current density in the bottom part of the EBM specimen compared with that of the cast specimen indicates a higher passive film stability of the former in the current corrosive environment. A larger pitting overpotential ($E_{pit} - E_{corr}$) for the bottom part of the EBM specimen than the cast counterpart also suggested the enhanced corrosion resistance. However, once stable pits nucleated on the EBM specimen surface, they grew more rapidly than those on the cast specimen. Repassivation was not obtained at either build height of the EBM specimen, as indicated by the cyclic polarisation tests.

Generally, the formation of pits in AlCoCrFeNi-based HEAs is closely related to a weakening of the passive films on the Cr-depleted region. That is, the Cr-depleted dendrites in the cast specimen suffered from serious preferential dissolution, whereas the Cr-rich interdendritic regions remained largely resistant to corrosion[22,24]. This is consistent with the morphology of the corroded surface for the cast specimen, as shown in Fig. 4c. Conversely, such a dendritic-scale dissolution was completely suppressed in the EBM counterparts (Fig. 4a, b), because the rapid cooling during EBM, in principle, allows the production of components that are essentially free of segregations at interdendritic regions[33]. Notably, the pitting corrosion of the EBM and cast specimens proceeded in the modulated BCC/B2 matrix via a phase-specific selective dissolution at the nanoscale, as shown in Fig. 4d–f. Therefore, this enhanced the resistance to pitting corrosion at the bottom part of the EBM specimen in comparison with the cast counterpart. The suppression of the dendritic-scale

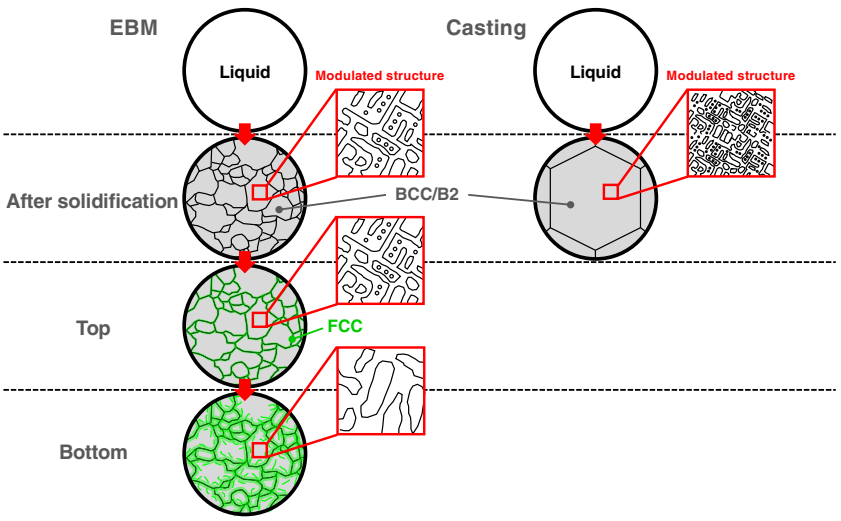

Fig. 8 Schematic showing the microstructural evolution of the equiatomic AlCoCrFeNi HEA during EBM and casting. The modulated BCC/B2 matrix and the FCC phase are represented in gray and green, respectively.

pitting corrosion has been observed in the homogenisation of AlCoCrFeNi-based HEAs[30]. Such a microstructural difference could be an origin for the reduced repassivation ability in the EBM specimen during cyclic polarisation (Fig. 3b, c) when compared with the cast specimen, although further study is required to clarify the underlying mechanism.

The pitting corrosion of the EBM specimen correlates with the nanoscale elemental partitioning during fabrication. The quantitative STEM-EDS elemental analysis (Table 1) revealed that the B2 phase in the EBM specimen had a much lower Cr content (less than 10 at%) than the BCC phase (approximately 50 at%). Furthermore, the FCC phase at both sections of the EBM specimen had a similar Cr content ($20-30$ at%). Thus, it is highly likely that the passive films are formed on the BCC and FCC phases of the alloy substrates. This hypothesis is reasonable because the XPS surface analysis detected an increase in the Cr^{3+} component during the static immersion (Fig. 7) and this correlated with the corroded surface observations that showed reduced corrosion during the polarisation tests (Fig. 4). Therefore, the selective dissolution that occurred at the Cr-lean, Al–Ni-enriched B2 phase must be a controlling process of the pitting corrosion, and this could explain why a continuous increase in the current density during the anodic polarisation occurred in the top sample.

An interesting observation that aids understanding of the enhanced corrosion resistance at the bottom part is the microstructural evolution during the 'in situ annealing' in the EBM process. The microstructural characterisation (Figs. 1 and 2) revealed that the bottom part had a higher FCC fraction and a weaker $\langle 100\rangle_{BCC/B2}$ texture evolution when compared with the top part. Furthermore, the modulated BCC/B2 matrix was coarser at the bottom part. The phase distributions and crystallographic texture are possible influencing factors of the corrosion performance of metals[60–62]. Notably, these microstructural evolutions are associated with the elemental partitioning between the constitutive phases (Table 1). Importantly, in the modulated BCC/B2 matrix, where corrosion occurred, the bottom part had a higher Cr content in the B2 phase than in the top part. Thus, a more severe dissolution at the B2 phase can be expected at the top part, hindering the passive region in the polarisation curve. This means that the redistribution of Cr that occurred with prolonged high-temperature exposure during the EBM process is essential for the corrosion performance. The spikes on the E_{oc} curve of the bottom specimen can be correlated to the metastable pitting caused by the above-mentioned phase-specific selective dissolution. However, the surface chemistry variation originating from the phase-specific corrosion could not be detected by the XPS analysis, because the quantitative values determined by the XPS analysis were averaged over the analysed area ($300\times700\,\mu m^2$), which is much larger than the microstructural length as mentioned above.

Nonetheless, the corrosion behaviour and passive film characteristics depended significantly on the bulk of microstructures, as successfully captured by the EIS analysis (Fig. 5). The results indicated that although an identical EEC could be adapted for all the specimens prepared in this work, the EIS parameters of each specimen showed apparent differences. For example, the charge-transfer resistance (R_{ct}) was much higher at the bottom part of the EBM specimen, and lowest at the top. Polarisation resistance (R_p), which is generally used to estimate the corrosion resistance and is inversely proportionate to the corrosion rate, is described as follows:

$$R_p = R_f + R_{ct}. \tag{1}$$

The R_p values for the studied specimens are shown in Table 3. While the R_f values of the specimens are almost identical, the R_{ct} value of the bottom part is more than one order of magnitude higher than the R_f value. This indicates that charge transfer is a critical factor for determining the electrochemical performance of the passive film. Consequently, the polarisation resistance of the bottom part of the EBM specimen was almost one order of magnitude larger than that of the top part, and three times larger than that of the cast specimen.

On the other hand, a lower Q value for the bottom part indicates the formation of a more homogeneous and less defective oxide film on the surface than that on the top part[63]. Furthermore, an effective capacitance (C_{eff}) can be obtained from the CPE parameters using the following equation[64–66]:

$$C_{eff} = \frac{(Q\cdot R)^{1/n}}{R}. \tag{2}$$

C_{eff} can be related to the thickness (t) of the passive film using the following equation[65]:

$$C_{eff} = \frac{\varepsilon\cdot\varepsilon_0}{t}, \tag{3}$$

where ε is the relative dielectric constant of the layer and ε_0 is the permittivity of vacuum ($8.85\times10^{-14}\,F\,cm^{-1}$). Equation (2) was constructed for an EEC with a singular time constant. However, Mohanmedi et al.[67] calculated the C_{eff} values for the EEC in Fig. 5c using the solution resistance (R_s), as follows[68]:

$$C_{eff} = \frac{(Q_f\cdot R_s)^{1/n_f}}{R_s}. \tag{4}$$

Mohanmedi et al.[67] confirmed the validity of Eq. (4) by comparing the film thickness determined by EIS parameters with those measured through ellipsometry. The C_{eff} values of the passive films formed on the samples used in the present study were also calculated. The results are shown in Table 3. The bottom sample possessed the lowest C_{eff} value among the studied samples, which was less than half of that of the top part, and the cast sample falls in the middle; this trend agreed well with the corrosion behaviour deduced from the polarisation tests. As the C_{eff} value is inversely proportional to the thickness of the passive film, the lowest Q_f and highest C_{eff} values in the bottom sample suggest the formation of a more homogeneous, compact, less defective passive film at the bottom section when immersed into the NaCl solution. The superior corrosion performance of the bottom part compared with that of the top part and the cast specimen can be explained by the more protective passive film formation and the enhanced R_p value.

Moreover, both Q_{dl} and n_{dl} values also varied depending on the samples. Qiu et al.[19] reported a high Q_{dl} value, which was similar to those for the top and bottom samples in this study, for pure Al immersed into a 0.6 M NaCl solution, whereas the single-phase AlTiVCr CCA with a better corrosion resistance had a much smaller value. The relatively small n_{dl} values for the present specimens imply local heterogeneities in the surface oxide film[69], although the bottom sample showed the highest value among the studied samples. Therefore, the subcircuit consisting of Q_{dl} and n_{dl} could be correlated with the B2 phase, which suffered from selective dissolution. The much lower Q_{dl} and slightly higher n_{dl} values for the bottom part of the EBM specimen would reflect the better corrosion resistance of the B2 phase among the studied samples. Conversely, the Q_f and n_f values seem to describe predominantly the passive film on the BCC and FCC phases, and the EEC model employed in this study suitably characterised the inhomogeneous passive films and the phase-specific selective corrosion behaviour.

The phase-specific pitting corrosion in AlCoCrFeNi-based HEAs can be described in terms of galvanic coupling between the constitutive phases[21,23]. Using scanning Kelvin probe force microscopy, Shi et al.[30] revealed an electrochemical potential difference between the BCC, B2 and FCC phases in the AlCoCrFeNi-based HEAs. The magnitude of the potential difference as a driving force for the nanoscale galvanic corrosion would depend on the composition, size and fraction of each constitutive phase, which could be affected by the building conditions.

Table 4. Chemical compositions of the EBM and cast equiatomic AlCoCrFeNi HEA specimens (at%).

	Al	Co	Cr	Fe	Ni	O
EBM	20.6	20.0	18.8	20.2	20.0	0.14
Cast	19.9	20.2	19.5	20.2	20.1	0.17

These findings clearly indicate that the microstructural evolution caused by 'in situ annealing' during the EBM process significantly influences the corrosion behaviour of the present HEA. In other words, rapidly solidified microstructures that are obtained by SLM and directed energy deposition, for instance, are similar to those observed in the top part of the EBM specimen, and are not always preferred if a high corrosion resistance is desired. Moreover, in terms of solidification segregation, the alloy microstructure at the bottom part must be different from the simply annealed coarse dendritic microstructures obtained by conventional casting. According to the microstructural observations and Vickers hardness measurements[35], the microstructure that was not exposed to post melting at high temperatures during the EBM process, which should be avoided if good corrosion performance is to be achieved (i.e. the microstructure referred to as the 'top part' in this study), existed only near the top part (2 mm in height), and most parts of the specimens were homogeneous and had microstructures similar to that of the 'bottom part'. This suggests that EBM is a promising method for optimising the corrosion performance of almost all parts of the structural components of HEAs.

METHODS

Sample preparation

Specimens examined in this study were produced by EBM and conventional casting. An Arcam A2X system (Arcam AB, Sweden) with an acceleration voltage of 60 kV was used to manufacture specimens with 20-mm × 20-mm × 16-mm dimensions from a gas-atomised powder (the particle size ranged from 45 to 105 µm). The preheating temperature was set to 950 °C. For comparison, cast specimens (15 mm in diameter and 300 mm in height) were also prepared by melting the same powder using a high-frequency induction furnace and a water-cooled copper mould. The chemical compositions of the EBM and cast specimens are shown in Table 4. The preparation processes have been previously described in detail[35]. The 'top' and 'bottom' specimens used in this paper were taken from locations 1 mm below the top and 1 mm above the bottom of the EBM specimens, respectively.

Microstructural characterisation

XRD (X'Pert MPD, PANalytical, Netherlands) was conducted using monochromatised Cu-*Kα* radiation to analyse the phase and structure of the alloys. The scanning range is from $2\theta = 20°$ to 100°, and the step size is 0.08°. SEM was conducted on a JSM-7100F microscope (JEOL, Japan) with a field-emission gun operated at 15 kV. Field-emission SEM (XL30S-FEG, FEI, USA) at 20 kV was used for EBSD analyses. A TSL-OIM system (version 7.3, EDAX, USA) was used to collect and analyse the EBSD data with a step size of 0.25 or 2.5 µm, according to the magnification. The microstructural characterisations of the EBM samples were conducted on the specimen cross-section in a direction perpendicular to the build direction. Samples for microstructural analyses were ground with emery paper, polished with a 1-µm alumina suspension and then finished with a 0.04-µm colloidal silica suspension (OP-S, Struers, Japan).

A TITAN^3 G2 60–300S/TEM (FEI, USA) with a spherical aberration (Cs) corrector operating at 300 kV was used for HAADF-STEM observations and EDS mapping. The samples for observation were obtained by cutting 3-mm-diameter disks from the top and bottom sections of the EBM specimens and then grinding them with a dimple grinder (Model 656, Gatan, USA) to form a thin film. After that, thin foils were formed by ion-beam milling (Model 691, PIPS, Gatan, USA).

Electrochemical characterisation

Electrochemical tests, including potentiodynamic polarisation and EIS, were performed using an SP-200 system (Bio-Logic Science Instruments, France) on a three-electrode flat cell consisting of a Pt mesh and Ag/AgCl electrode as the counter and reference electrodes, respectively. The samples with a measurement area of 1 cm^2, which were cut from the top and bottom sections of the as-built materials and the as-cast counterparts, were used as working electrodes. Before each measurement, the samples were ground with 1000-grit emery paper, cleaned with acetone and dried with compressed air. The measurements were performed in a 3.5 wt% NaCl solution at room temperature (~25 °C). The test solutions (~250 mL) were exposed to air during the measurements. After the polarisation tests, the surfaces were observed by SEM (JSM-7100F, JEOL, Japan) operated at 15 kV.

For each specimen, the E_{oc} was measured for up to 6 h. The specimens were then anodically polarised within the range of −0.3 V vs. E_{oc} to 0.5 V vs. Ag/AgCl at the scan rate of 1 mV s^{-1}. In order to investigate the susceptibility of the prepared alloy specimens to localised corrosion attacks (namely, pitting corrosion), cyclic potentiodynamic polarisation tests were performed from an initial potential of −0.3 V vs. E_{oc} to a potential of 0.5 V vs. Ag/AgCl at forward and reverse scan rates of 1 mV s^{-1} with a peak current density of 5 mA cm^{-2}. The obtained data were analysed using the EC-Lab® software (Bio-Logic Science Instruments, France).

The EIS measurements were performed after 6-h immersion at an amplitude of 10 mV at E_{oc} in the frequency range of 100 kHz–10 mHz. In the EEC, the impedance of a CPE is defined as[69]

$$Z_{CPE} = \frac{1}{(j\omega)^n Q}, \quad (5)$$

where the exponent n $(-1 \le n \le 1)$ is a coefficient that describes the deviation between the real capacitance and pure capacitance. Q and ω represent the general admittance function and the angular frequency, respectively. The CPE for $n = 1$ and 0 describes an ideal capacitor and an ideal resistor, respectively. The CPE for $n = 0.5$ represents a Warburg impedance with diffusional character. Finally, the CPE for $0.5 < n < 1$ describes a frequency dispersion of time constants due to local heterogeneities in the dielectric material. A pure inductance yields $n = -1$.

Surface characterisation

Oxidation states and compositions of the surface oxide films were analysed before and after the immersion of the specimens in a 3.5 wt% NaCl solution for 6 h. For the analysis, XPS (Axis Ultra DLD, Shimadzu-Kratos, UK) was performed using monochromatised Al *Kα* X-ray radiation (15 kV, 10 mA) with an excitation energy of 1486.7 eV. The instrument was calibrated to give an Au $4f_{7/2}$ metallic gold BE of 84.0 ± 0.1 eV. The spectrometer dispersion was adjusted to give a BE of 932.6 ± 0.1 eV for metallic Cu $2p_{3/2}$. A 300 × 700-µm area of the sample was analysed by XPS. The survey and narrow scans were made in 1 and 0.1-eV step sizes, respectively. The pass energy for collecting the survey and narrow spectra were 160 or 40 eV, respectively. Spectra from insulating samples were charge-corrected to give the adventitious C *1s* signal at a binding energy of 284.8 eV. The chemical states of the elements were determined from the peak positions obtained by deconvoluting the high-resolution scan spectra. Spectra were analysed using CasaXPS software (ver. 2.3.15). A standard Shirley (or often linear) background was used for all reference samples of the spectra. Positions and the full width at half maximum (FWHM) of each peak are summarised in Supplemental Tables 1−3. The energy shifts as well as the FWHMs indicated an acceptable fit for all angles and potentials. The immersed alloy samples were cleaned with distilled water and then dried with air before the XPS measurements.

DATA AVAILABILITY

The datasets generated and/or analysed during the current study are available from the corresponding author upon reasonable request.

Received: 13 April 2020; Accepted: 10 July 2020;
Published online: 11 August 2020

REFERENCES

1. Yeh, J.-W. et al. Nanostructured high-entropy alloys with multiple principal elements: Novel alloy design concepts and outcomes. *Adv. Eng. Mater.* **6**, 299–303 (2004).

2. Cantor, B., Chang, I. T. H., Knight, P. & Vincent, A. J. B. Microstructural development in equiatomic multicomponent alloys. *Mater. Sci. Eng. A* **375–377**, 213–218 (2004).
3. Zhang, Y. et al. Microstructures and properties of high-entropy alloys. *Prog. Mater. Sci.* **61**, 1–93 (2014).
4. Oh, H. S. et al. Lattice distortions in the FeCoNiCrMn high entropy alloy studied by theory and experiment. *Entropy* **18**, 321–321 (2016).
5. Li, Z., Pradeep, K. G., Deng, Y., Raabe, D. & Tasan, C. C. Metastable high-entropy dual-phase alloys overcome the strength–ductility trade-off. *Nature* **534**, 227–230 (2016).
6. Zhang, Z. et al. Nanoscale origins of the damage tolerance of the high-entropy alloy CrMnFeCoNi. *Nat. Commun.* **6**, 10143 (2015).
7. Gludovatz, B. et al. A fracture-resistant high-entropy alloy for cryogenic applications. *Science* **345**, 1153–1158 (2014).
8. Chuang, M. H., Tsai, M. H., Wang, W. R., Lin, S. J. & Yeh, J. W.Microstructure and wear behavior of $Al_xCo_{1.5}CrFeNi_{1.5}Ti_y$ high-entropy alloys. *Acta Mater.* **59**, 6308–6317 (2011).
9. Hsu, C.-Y., Sheu, T.-S., Yeh, J.-W. & Chen, S.-K. Effect of iron content on wear behavior of $AlCoCrFe_xMo_{0.5}Ni$ high-entropy alloys. *Wear* **268**, 653–659 (2010).
10. Wang, X. F., Zhang, Y., Qiao, Y. & Chen, G. L. Novel microstructure and properties of multicomponent $CoCrCuFeNiTi_x$ alloys. *Intermetallics* **15**, 357–362 (2007).
11. Shun, T. T., Chang, L. Y. & Shiu, M. H. Microstructures and mechanical properties of multiprincipal component $CoCrFeNiTi_x$ alloys. *Mater. Sci. Eng. A* **556**, 170–174 (2012).
12. Jensen, J. K. et al. Characterization of the microstructure of the compositionally complex alloy $Al_1Mo_{0.5}Nb_1Ta_{0.5}Ti_1Zr_1$. *Scr. Mater.* **121**, 1–4 (2016).
13. Qiu, Y. et al. A lightweight single-phase AlTiVCr compositionally complex alloy. *Acta Mater.* **123**, 115–124 (2017).
14. Li, Y. J., Savan, A., Kostka, A., Stein, H. S. & Ludwig, A. Accelerated atomic-scale exploration of phase evolution in compositionally complex materials. *Mater. Horiz.* **5**, 86–92 (2018).
15. Lin, C. M., Tsai, H. L. & Bor, H. Y. Effect of aging treatment on microstructure and properties of high-entropy $Cu_{0.5}CoCrFeNi$ alloy. *Intermetallics* **18**, 1244–1250 (2010).
16. Chen, Y. Y., Duval, T., Hung, U. D., Yeh, J. W. & Shih, H. C. Microstructure and electrochemical properties of high entropy alloys-a comparison with type-304 stainless steel. *Corros. Sci.* **47**, 2257–2279 (2005).
17. Chen, Y. Y., Hong, U. T., Shih, H. C., Yeh, J. W. & Duval, T. Electrochemical kinetics of the high entropy alloys in aqueous environments—a comparison with type 304 stainless steel. *Corros. Sci.* **47**, 2679–2699 (2005).
18. Chou, Y. L., Wang, Y. C., Yeh, J. W. & Shih, H. C. Pitting corrosion of the high-entropy alloy $Co_{1.5}CrFeNi_{1.5}Ti_{0.5}Mo_{0.1}$ in chloride-containing sulphate solutions. *Corros. Sci.* **52**, 3481–3491 (2010).
19. Qiu, Y. et al. Microstructure and corrosion properties of the low-density single-phase compositionally complex alloy AlTiVCr. *Corros. Sci.* **133**, 386–396 (2018).
20. Kumar, N. et al. Understanding effect of 3.5 wt.% NaCl on the corrosion of $Al_{0.1}CoCrFeNi$ high-entropy alloy. *J. Nucl. Mater.* **495**, 154–163 (2017).
21. Ayyagari, A. V., Gwalani, B., Muskeri, S., Mukherjee, S. & Banerjee, R. Surface degradation mechanisms in precipitation-hardened high-entropy alloys. *npj Mater. Degrad.* **2**, 33 (2018).
22. Li, Q. H., Yue, T. M., Guo, Z. N. & Lin, X. Microstructure and corrosion properties of AlCoCrFeNi high entropy alloy coatings deposited on AISI 1045 steel by the electrospark process. *Metall. Mater. Trans. A* **44A**, 1767–1778 (2013).
23. Shi, Y. et al. Corrosion of $Al_xCoCrFeNi$ high-entropy alloys: Al-content and potential scan-rate dependent pitting behavior. *Corros. Sci.* **119**, 33–45 (2017).
24. Xiang, C. et al. Microstructure and corrosion behavior of $AlCoCrFeNiSi_{0.1}$ high-entropy alloy. *Intermetallics* **114**, 106599 (2019).
25. Chou, Y. L., Yeh, J. W. & Shih, H. C. The effect of molybdenum on the corrosion behaviour of the high-entropy alloys $Co_{1.5}CrFeNi_{1.5}Ti_{0.5}Mo_x$ in aqueous environments. *Corros. Sci.* **52**, 2571–2581 (2010).
26. Kao, Y. F., Lee, T. D., Chen, S. K. & Chang, Y. S. Electrochemical passive properties of $Al_xCoCrFeNi$ ($x = 0$, 0.25, 0.50, 1.00) alloys in sulfuric acids. *Corros. Sci.* **52**, 1026–1034 (2010).
27. Lee, C. P., Chang, C. C., Chen, Y. Y., Yeh, J. W. & Shih, H. C. Effect of the aluminium content of $Al_xCrFe_{1.5}MnNi_{0.5}$ high-entropy alloys on the corrosion behaviour in aqueous environments. *Corros. Sci.* **50**, 2053–2060 (2008).
28. Lee, C. P., Chen, Y. Y., Hsu, C. Y., Yeh, J. W. & Shih, H. C. The effect of boron on the corrosion resistance of the high entropy alloys $Al_{0.5}CoCrCuFeNiB_x$. *J. Electrochem. Soc.* **154**, C424–C430 (2007).
29. Lin, C. M. & Tsai, H. L. Evolution of microstructure, hardness, and corrosion properties of high-entropy $Al_{0.5}CoCrFeNi$ alloy. *Intermetallics* **19**, 288–294 (2011).
30. Shi, Y. et al. Homogenization of $Al_xCoCrFeNi$ high-entropy alloys with improved corrosion resistance. *Corros. Sci.* **133**, 120–131 (2018).
31. Qiu, Y., Gibson, M. A., Fraser, H. L. & Birbilis, N. Corrosion characteristics of high entropy alloys. *Mater. Sci. Technol.* **31**, 1235–1243 (2015).
32. Qiu, Y., Thomas, S., Gibson, M. A., Fraser, H. L. & Birbilis, N. Corrosion of high entropy alloys. *npj Mater. Degrad.* **1**, 15 (2017).
33. Körner, C. Additive manufacturing of metallic components by selective electron beam melting—a review. *Int. Mater. Rev.* **61**, 361–377 (2016).
34. Fujieda, T. et al. First demonstration of promising selective electron beam melting method for utilizing high-entropy alloys as engineering materials. *Mater. Lett.* **159**, 12–15 (2015).
35. Shiratori, H. et al. Relationship between the microstructure and mechanical properties of an equiatomic AlCoCrFeNi high-entropy alloy fabricated by selective electron beam melting. *Mater. Sci. Eng. A* **656**, 39–46 (2016).
36. Kuwabara, K. et al. Mechanical and corrosion properties of AlCoCrFeNi high-entropy alloy fabricated with selective electron beam melting. *Addit. Manuf.* **23**, 246–271 (2018).
37. Zhang, H. et al. Manufacturing and analysis of high-performance refractory high-entropy alloy via selective laser melting (SLM). *Materials* **12**, 720 (2019).
38. Fujieda, T. et al. CoCrFeNiTi-based high-entropy alloy with superior tensile strength and corrosion resistance achieved by a combination of additive manufacturing using selective electron beam melting and solution treatment. *Mater. Lett.* **189**, 148–151 (2017).
39. Fujieda, T. et al. Mechanical and corrosion properties of CoCrFeNiTi-based high-entropy alloy additive manufactured using selective laser melting. *Addit. Manuf.* **25**, 412–420 (2019).
40. Sarswat, P. K. et al. Additive manufactured new hybrid high entropy alloys derived from the AlCoFeNiSmTiVZr system. *Appl. Surf. Sci.* **476**, 242–258 (2019).
41. Sochalski-Kolbus, L. M. et al. Comparison of residual stresses in inconel 718 simple parts made by electron beam melting and direct laser metal sintering. *Metall. Mater. Trans. A* **46**, 1419–1432 (2015).
42. Yamanaka, K. et al. Abnormal grain growth of commercially pure titanium during additive manufaturing with electron beam melting. *Materialia* **6**, 100281 (2019).
43. Sun, S. H., Koizumi, Y., Kurosu, S., Li, Y. P. & Chiba, A. Phase and grain size inhomogeneity and their influences on creep behavior of Co−Cr−Mo alloy additive manufactured by electron beam melting. *Acta Mater.* **86**, 305–318 (2015).
44. Sames, W. J. et al. Feasibility of in situ controlled heat treatment (ISHT) of Inconel 718 during electron beam melting additive manufacturing. *Addit. Manuf.* **13**, 156–165 (2017).
45. Munitz, A., Salhov, S., Hayun, S. & Frage, N. Heat treatment impacts the microstructure and mechanical properties of AlCoCrFeNi high entropy alloy. *J. Alloy. Compd.* **683**, 221–230 (2016).
46. Tang, Z. et al. Tensile ductility of an AlCoCrFeNi multi-phase high-entropy alloy through hot isostatic pressing (HIP) and homogenization. *Mater. Sci. Eng. A* **647**, 229–240 (2015).
47. Manzoni, A., Daoud, H., Völkl, R., Glatzel, U. & Wanderka, N. Phase separation in equiatomic AlCoCrFeNi high-entropy alloy. *Ultramicroscopy* **132**, 212–215 (2013).
48. Qiu, Y. et al. Microstructural evolution, electrochemical and corrosion properties of $Al_xCoCrFeNiTi_y$ high entropy alloys. *Mater. Des.* **170**, 107698 (2019).
49. Wilde, B. E. A critical appraisal of some popular laboratory electrochemical tests for predicting the localized corrosion resistance of stainless alloys in sea water. *Corrosion* **28**, 283–291 (1972).
50. Bommersbach, P., Alemany-Dumont, C., Millet, J. P. & Normand, B. Formation and behaviour study of an environment-friendly corrosion inhibitor by electrochemical methods. *Electrochim. Acta* **51**, 1076–1084 (2005).
51. Wang, W. et al. Effect of Mo and aging temperature on corrosion behavior of $(CoCrFeNi)_{100-x}Mo_x$ high-entropy alloys. *J. Alloy. Compd.* **812**, 152139 (2020).
52. Oltra, R. & Keddam, M. Application of impedance technique to localized corrosion. *Corros. Sci.* **28**, 7–18 (1988).
53. Hodgson, A. W. E. et al. Passive and transpassive behaviour of CoCrMo in simulated biological solutions. *Electrochim. Acta* **49**, 2167–2178 (2004).
54. Hanawa, T. Metal ion release from metal implants. *Mater. Sci. Eng. C* **24**, 745–752 (2004).
55. Mori, M. et al. Effect of carbon on the microstructure, mechanical properties and metal ion release of Ni-free Co–Cr–Mo alloys containing nitrogen. *Mater. Sci. Eng. C* **55**, 145–154 (2015).
56. Yamanaka, K. et al. Effect of multipass thermomechanical processing on the corrosion behaviour of biomedical Co–Cr–Mo alloys. *Corros. Sci.* **148**, 178–187 (2019).
57. Borkar, T. et al. A combinatorial approach for assessing the magnetic properties of high entropy alloys: role of Cr in $AlCo_xCr_{1-x}FeNi$. *Adv. Eng. Mater.* **19**, 1700048 (2017).
58. Wang, R., Zhang, K., Davies, C. & Wu, X. Evolution of microstructure, mechanical and corrosion properties of AlCoCrFeNi high-entropy alloy prepared by direct laser fabrication. *J. Alloy. Compd.* **694**, 971–981 (2017).

59. Zhang, C. et al. Understanding phase stability of Al-Co-Cr-Fe-Ni high entropy alloys. *Mater. Des.* **109**, 425–433 (2016).
60. Tsai, W. T. & Chen, J. R. Galvanic corrosion between the constituent phases in duplex stainless steel. *Corros. Sci.* **49**, 3659–3668 (2007).
61. Hoseini, M., Shahryari, A., Omanovic, S. & Szpunar, J. A. Comparative effect of grain size and texture on the corrosion behaviour of commercially pure titanium processed by equal channel angular pressing. *Corros. Sci.* **51**, 3064–3067 (2009).
62. Obayi, C. S. et al. Influence of cross-rolling on the micro-texture and biodegradation of pure iron as biodegradable material for medical implants. *Acta Biomater.* **17**, 68–77 (2015).
63. MacDonald, D. D. The history of the point defect model for the passive state: a brief review of film growth aspects. *Electrochim. Acta* **56**, 1761–1772 (2011).
64. Kocijan, A., Merl, D. K. & Jenko, M. The corrosion behaviour of austenitic and duplex stainless steels in artificial saliva with the addition of fluoride. *Corros. Sci.* **53**, 776–783 (2011).
65. Hirschorn, B. et al. Determination of effective capacitance and film thickness from constant-phase-element parameters. *Electrochim. Acta* **55**, 6218–6227 (2010).
66. Valero Vidal, C. & Igual Muñoz, A. Study of the adsorption process of bovine serum albumin on passivated surfaces of CoCrMo biomedical alloy. *Electrochim. Acta* **55**, 8445–8452 (2010).
67. Mohammadi, F., Nickchi, T., Attar, M. M. & Alfantazi, A. EIS study of potentiostatically formed passive film on 304 stainless steel. *Electrochim. Acta* **56**, 8727–8733 (2011).
68. Brug, G. J., van den Eeden, A. L. G., Sluyters-Rehbach, M. & Sluyters, J. H. The analysis of electrode impedances complicated by the presence of a constant phase element. *J. Electroanal. Chem.* **176**, 275–295 (1984).
69. Jorcin, J.-B., Orazem, M. E., Pébère, N. & Tribollet, B. CPE analysis by local electrochemical impedance spectroscopy. *Electrochim. Acta* **51**, 1473–1479 (2006).

ACKNOWLEDGEMENTS

The authors thank Yuichiro Hayasaka (Institute for Materials Research, Tohoku University) for TEM observations. This research was partly supported by Grants-in-Aid for Young Scientist (A) [Grant No. 17H04957] and the Grant-in-Aid for Scientific Research on Innovative Area 'High Entropy Alloys' [Grant No. 18H05455], both from the Japan Society for the Promotion of Science (JSPS), and the Grant-in-Aid for Scientific Research in a Priority Area on 'Creation of Life Innovation Materials for Interdisciplinary and International Researcher Development' from the Ministry of Education, Culture, Sports, Science and Technology of Japan. The XPS analysis was conducted at the Cooperative Research and Development Center for Advanced Materials, Institute for Materials Research, Tohoku University [Proposal nos. 19G0414 and 20G0416].

AUTHOR CONTRIBUTIONS

K.Y. and A.C. conceived the project and designed the experiments. K.Y., H.S., M.M. and K.O. performed the experiments and analyses. T.F. and K.K. contributed to the preparation of alloy specimens. K.Y. wrote the paper. H.S., M.M. and K.O. revised the paper. All the authors contributed to the interpretation of the experimental data and discussed the results.

COMPETING INTERESTS

The authors declare no competing interests.

ADDITIONAL INFORMATION

Supplementary information is available for this paper at https://doi.org/10.1038/s41529-020-00127-4.

Correspondence and requests for materials should be addressed to K.Y.

Reprints and permission information is available at http://www.nature.com/reprints

Publisher's note Springer Nature remains neutral with regard to jurisdictional claims in published maps and institutional affiliations.